Electrocatalysis (2023) 14:55–67
https://doi.org/10.1007/s12678-022-00772-0

ORIGINAL RESEARCH

Highly Active Lanthanum Perovskite Electrocatalysts ($LaMn_xCo_{1-x}O_3$ ($0 \le x \le 1$)) by Tuning the Mn:Co Ratio for ORR and MOR in Alkaline Medium

Sadiyah Shafath[1] · Khulood Logade[1] · Anchu Ashok[1] · Anand Kumar[1] · Ibrahim M. Abu-Reesh[1]

Accepted: 22 August 2022 / Published online: 8 September 2022

Abstract

Lanthanum-based perovskites ($LaMn_xCo_{1-x}O_3$ ($0 \le x \le 1$)) were synthesized using a solution combustion synthesis technique with variable ratios of Co and Mn to investigate the surface property and electrocatalytic characteristics (stability and activity of catalyst) for methanol oxidation reaction (MOR), oxygen reduction reaction (ORR), and oxygen evolution reaction (OER) under alkaline medium (KOH). The structural, chemical, and morphological characterizations of the synthesized catalyst were performed by XRD, FTIR, SEM, TEM, and XPS techniques as a function of the Mn:Co elemental ratio. The time–temperature profile during the combustion process was also monitored to study the completion of the combustion reaction and to understand its impact on the structure of the perovskites. SEM/EDX and XPS analysis confirmed the formation of the targeted ratio of Mn and Co on the catalyst. Cyclic voltammetry (CV) and linear sweep voltammetry (LSV) results revealed that all perovskite samples with different Co:Mn ratios were active for ORR, OER, and MOR. The $LaMn_xCo_{1-x}O_3$ perovskite with $x = 0.4$ showed the highest current density compared to the other samples toward all the electrocatalytic reactions under alkaline reaction conditions.

Keywords Lanthanum perovskites · Solution combustion synthesis · Electrocatalysts · Oxygen reduction reaction · Oxygen evolution reaction · Methanol oxidation

Introduction

The current global energy crisis is demanding the development of a more economical, efficient, and environmentally friendly energy system to deal with the environmental effect of oil supply. Electrochemical fuel cells have the potential to provide a more ecological and efficient alternative to conventional power sources such as fossil fuels [1]. Therefore, steady progress in fuel cell development has been observed over the past decades due to advantages like low expenses, low operating temperature, as well as high energy conversion efficiency [2–4]. Direct methanol fuel cells (DMFCs) are simple, compact, and have high energy density, making them a desirable power source [5]. However, their large-scale usage requires more effective, economic, and stable catalysts to perform the energy conversion operation with high efficiency at a lower cost, and in an uninterrupted manner [6]. To further boost the charge transport through the cell, an electrocatalyst with high electrical conductivity and corrosion resistance properties under an intense electrochemical environment is required [7]. These characteristics are necessary for catalysts to have any industrial relevance, particularly the long-term stability and abundance of material to scale up the overall processes to the industrial level [8–10]. Several possible catalysts, such as those that are lanthanum based, cobalt based, platinum based, or silver based, have been employed for these cells. In many cases, bimetallic catalysts are found to be more efficient than the individual constituents for actively transforming methanol to produce energy. Utilizing these catalysts in DMFCs involves the oxidation of methanol on the surface of the catalyst to

Sadiyah Shafath and Khulood Logade equally contributed to this article.

✉ Anand Kumar
akumar@qu.edu.qa

✉ Ibrahim M. Abu-Reesh
abureesh@qu.edu.qa

[1] Department of Chemical Engineering, College of Engineering, Qatar University, P O Box 2713, Doha, Qatar

produce carbon dioxide [11–14]. The electrooxidation process occurs on the anode and follows the below equation:

$$CH_3OH + H_2O \rightarrow 6H^+ + CO_2 + 6e- \quad (1)$$

The reaction taking place on the cathode side, ORR, is expressed as [15]

$$O_2 + H_2O + 4e- \rightarrow 4OH- \quad (2)$$

Chen et al. (2020) tested Pt–Co nanoframes for fuel cell electrocatalysis and found them to be promising candidates for ORR and MOR reactions [16]. Antolini et al. studied the results of Pt–Co and Pt–Ni catalysts in DMFC and found encouraging results for MOR in the presence of a low amount of non-precious metal [17]. However, one of the main drawbacks of DMFCs is the very slow anodic reaction, which, combined with an inefficient cathodic reaction, results in poor overall performance, especially at low temperatures [18, 19].

Currently, perovskite oxides have received great attention due to their flexibility and coordination of their physiochemical and catalytic properties, showing great potential in the DMFCs research field [20–25]. The A site of the perovskite oxides having a crystal structure of ABO_3 is a rare earth metal (either alkaline earth metals or lanthanides), and B corresponds to transition metals such as Mn, Cr, Fe, Ni, and Co. It has been reported that ABO_3 perovskites can be adequately modified by a partial replacement of atoms in A or B sites, which considerably improves the activity by imparting structural changes such as lattice distortions, stabilization of multiple oxidation states, or the generation of cationic and anionic vacancies [26, 27].

One major advantage of ABO_3 perovskites is that the crystal lattice of either A or B can be filled with several metals, which in turn can influence their catalytic properties [28, 29]. Ideally, the crystalline sites of A and B should be occupied by the same number of cations (A/B = 1), however, the electronic structure and the catalytic performance can be affected if the ideal condition is not observed [30]. It is quite possible to vary the interaction between the oxygenated species and the B-site specie to regulate the catalytic properties of the perovskites.

Erdenee et al. studied the effect of substituting La with a cation of higher valence, Ce as in $La_{1-x}Ce_xMnO_3$ and $La_{1-x}Ce_xCoO_3$, which displayed promising structural and catalytic properties [26]. Chen et al. prepared lanthanum-doped $BiFeO_3$ crystallites using the sol–gel hydrothermal method and discovered that the morphology and dimension of the BLFO microspheres and submicrotiles could be effectively controlled by varying KOH concentrations during synthesis [31]. Wen et al. investigated the oxidation properties of nitrogen monoxide over lanthanum perovskites with cerium substitution [32] and demonstrated the possibility of tuning perovskite properties by Ce substitution. The broad nature and family of perovskite oxides allow for varied investigations into the synthesis, properties, and catalytic performance of these materials.

In the current study, the surface and electrocatalytic performance (stability and activity of catalyst) for ORR, OER, and methanol oxidation reaction were studied under an alkaline medium over lanthanum-based synthetic perovskite ($LaMn_xCo_{1-x}O_3$ ($0 \le x \le 1$)) prepared using solution combustion synthesis technique. A combination of Mn and Co in variable ratios was selected as the B-site of the perovskites due to their higher activity and better selectivity reported in our earlier study [15]. The $LaMn_xCo_{1-x}O_3$ perovskites are chosen for this study to generate eco-friendly and cost-effective electrocatalysts suitable for producing energy in a stable and efficient manner, which will be useful in fuel cell applications.

Experimental

All the chemicals for this work were used in their purest form as purchased from the suppliers. Glycine ($C_2H_5NO_2$, 99.7%), lanthanum nitrate ($La(NO_3)_2{\cdot}6H_2O$, 99.99%), manganese (II) nitrate tetrahydrate ($Mn(NO)_3.4H_2O$, 97%), and cobalt (II) nitrate hexahydrate ($Co(NO_3)_2.6H_2O$,97%) were used as the initial reagents. Perfluorinated Nafion (5% in a mixture of lower aliphatic alcohols and water), isopropyl alcohol (99.7%), and methanol (99.8%) were also used as supplied. Deionized millipore water was used for all the experiments related to catalyst synthesis and electrocatalytic performance valuation.

Synthesis of Lanthanum Perovskites

$LaMn_xCo_{1-x}O_3$ perovskites were produced using a single-step solution combustion synthesis (SCS) technique. Based on a calculation to obtain 1 g of nanoparticles after the combustion reaction, precursors such as lanthanum nitrate, manganese (II) nitrate tetrahydrate, cobalt (II) nitrate hexahydrate, and glycine with a fuel ratio of $\varphi = 1$ were measured [15, 33–38]. The powders were dissolved in 25 ml of deionized (DI) water and stirred for 1 h to obtain homogeneous solutions, which were placed on a hot plate heater at 300 °C to evaporate excess water and initiate the combustion synthesis reaction to obtain the desired nanopowders. The obtained solids were hand ground and sieved with a 75 µm sieve to collect nanoparticles of uniform size < 75 µm. The prepared nanoparticles were dispersed in water with the addition of carbon black to ensure a high electrical conductivity during the electrochemical reaction. A 30 mg of the synthesized powdered perovskite was dispersed in 0.2 ml of DI water and well sonicated for 1 h, then 70 mg of carbon

black powder (Vulcan XC72) was slowly added to the solution. The produced perovskite/carbon solution was heated at 110 °C hot plate until the sample was dried, which was collected and hand ground to obtain La–M/C particles for electrocatalytic reactions.

Characterization

The particle synthesized underwent bulk phase identification with the help of Rigaku MiniFlex II Benchtop X-ray diffractometer (XRD) at 0.154056 nm wavelength of CuKα radiation having a scan range between 10 and 80°. A scanning electron microscope (Nova NanoSEM 450, FEI) with a magnification of up to × 200 in conjunction with EDX was used to perform the microstructure analysis and obtain the elemental composition. The size identification of the particle was performed using FEI Talos F200X TEM together with EDS (FEI SuperX EDS System) for elemental mapping and quantitative identification. X-ray photoelectron spectroscopy (XPS, Kratos AXIS Ultra DLD) was utilized to study the surface oxidation state of the elements in the samples and the reported binding energies (BEs) from the XPS data were calibrated with respect to C 1 s at 284.8 eV. In addition, Fourier transmission infrared (FTIR) analysis was performed using Thermo Scientific Spectrometer (Nicolet 6700) over a frequency range of 500–4000 cm^{-1}.

Electrochemical Measurement

The electrochemical behavior of the nanoparticles was measured by using a three-electrode system with PINE instruments bipotentiostat (WaveDriver 20), which was connected to a rotating disc electrode (RDE). A solution of 1 M KOH was used as an electrolyte to perform the electrochemical measurements at room temperature. The working, counter, and reference electrodes used for the experiment were catalyst-loaded glassy carbon disc (5 mm dia, 0.196 cm^2 area), platinum coil, and Ag/AgCl single junction electrodes, respectively. The preparation of the working electrode involved a dispersion of 10 mg of $LaMn_xCo_{1-x}O_3$/C in 2.5 ml of DI water followed by 1 h of sonication. The working electrode and the glassy carbon disc were then coated with 20 µl of the prepared ink, resulting in 24 µg of perovskites on the glassy carbon disc and 122.23 µg/cm^2 catalyst density. After the working electrode was dried up, 0.1% solution of Nafion was dropped on the glassy carbon to ensure that the catalyst sticks well on the surface of the disc. Firstly, the pretreatment and cyclic voltammetry (CV) of the working electrode were performed in an N_2-saturated electrolyte at a scan rate of 500 mV/s for 100 cycles and 50 mV/s for 6 cycles, respectively, both within the potential range of − 0.9 to 0.4 V. The electrolyte was saturated with O_2 by purging a high-purity O_2 for 1 h prior to the ORR. Linear sweep voltammetry (LSV) was measured between 0.9 and 0.8 V at a rotation between 400 and 1600 rpm at a scan rate of 5 mV/s. Koutecky–Levich plot was used to calculate the number of electron transfers (n) in the overall reaction using the slope of the KL equation:

$$\frac{1}{J} = \frac{1}{J_L} + \frac{1}{J_K} = \frac{1}{Bw^{1/2}} + \frac{1}{J_K} \tag{3}$$

$$B = 0.62nF\ C_0(D_0)^{2/3}\nu^{-1/6} \tag{4}$$

$$J_k = nFkC_0 \tag{5}$$

where J_K, J_L, and J are the kinetic current density, limiting current density, and measured current density. The measured current density was calculated by dividing the measured current by the geometric area of the working electrode (0.196 cm^2). Also, ω be the angular electrode rotation, n is the overall electron transfer, and k is the electron transfer rate constant. The constants in the equations used for the calculations are $F = 96485$C mol^{-1}, the bulk concentration of dissolved O_2 in the electrolyte, $C_0 = 7.8 \times 10^{-7}$ molcm^{-3} (1 M KOH), the υ kinematic viscosity of electrolyte is 0.01 $cm^2\ s^{-1}$, and D_0, the diffusion coefficient is 1.9×10^{-5} $cm^2\ s^{-1}$. Thereafter, 1 M methanol was added to the electrolyte in order to perform the MOR experiments.

Results and Discussion

The time–temperature profile during the solution combustion synthesis of samples was monitored for comparison purposes, as shown in Fig. S1, for all the $LaMn_xCo_{1-x}O_3$ perovskites with different values of x. This profile gives an insight into the synthesis conditions as the start of the combustion reaction is identified with the change in the temperature profile trend. The combustion temperature was found to be highest for $LaMn_{0.5}Co_{0.5}O_3$ (corresponding to 05:05 in Fig. S1) compared to other samples. Also, the tail of $LaMn_{0.8}Co_{0.2}O_3$ (corresponding to 08:02 in Fig. S1) after the combustion peak decreases slowly, hence it has a longer sintering time compared to other samples with a relatively sharp drop in temperature after combustion. Overall, perovskite powder for all the $LaMn_xCo_{1-x}O_3$ samples was obtained at a shorter reaction time (< 1000 s). Moreover, the combustion temperature of the samples was affected by the value of x (ratio of Mn:Co), which in turn affected the properties of each synthesized material. Thus, all $LaMn_xCo_{1-x}O_3$ samples differ from each other in terms of crystal formation temperature, sintering, nanoparticle growth, and associated physiochemical properties of the perovskites, such as crystallite size, surface area, and porosity.

Figure 1 shows the XRD analysis of the synthesized $LaMn_xCo_{1-x}O_3$ perovskites with different Mn–Co ratio. In $LaMn_{0·8}Co_{0·2}O_3$, the well crystalline peaks observed at 22.6° (110), 32.2° (200), 39.9° (202), 46.82° (220), 57.84° (222), 67.62° (312), and 76.86° (332) correspond to perovskite phase, agreeing with the formation of crystallites with ABO_3 structure. XRD profile of pure $LaCoO_3$ in Fig. 1 shows sharp crystalline peaks, while for $LaMnO_3$, the peaks were too broad. The XRD peak shifted to a lower angle with an increase in the manganese ratio, which can be attributed to an increase in cell dimension owing to a higher ionic radius of the doped manganese ions. In $LaMn_{0·6}Co_{0·4}O_3$, some trace of La_2O_3 was also identified. The crystalline peaks become broader owing to the smaller crystallite size with an increase in Co content as visible in $LaMn_{0.4}Co_{0.6}O_3$ and $LaMn_{0.2}Co_{0.8}O_3$. The crystallite size was calculated using Sherrer's equation varies from 6.5 and 32.5 nm for $LaMn_{0.4}Co_{0.8}O_3$ and $LaMn_{0.8}Co_{0.2}O_3$, respectively. Autret et al. studied the phase change in the perovskite structure of $LaMn_xCo_{1-x}O_3$ by varying the composition and Mn and Co content [39]. The diffraction pattern was indexed at orthorhombic perovskite structure for $x = 0$–0.5, and the structural transformations originate with an increase in Co content, with the unit cell parameters close to rhombohedral structure that is more resembled to $LaCoO_3$ perovskite.

Figure S2 shows the structural analysis of $LaMn_xCo_{1-x}O_3$ perovskites studied using FTIR spectroscopy. The broad band around 3000–3500 cm^{-1} corresponds to OH– stretching vibration and is an indication of the existence of moisture/entrapped water on the perovskite surface. The diffused band at 1400–1500 cm^{-1} indicates the δOH and γOH vibration of water molecules. The multiple infrared bands in the range of 500–900 cm^{-1} are allotted for different stretching modes of M–O bond on the metal oxide framework [40]. The FTIR peak at 550 cm^{-1} corresponds to the stretching vibration of the Mn–O bond (v_1 mode) and its intensity diminishes with an increase in the cobalt doping that confirms the elemental substitution of cobalt on manganese in the perovskite structure. Similarly, another FTIR peak around 780 cm^{-1} is attributed to the vibration of the Co–O bond, with the highest intensity for $LaMn_{0·2}Co_{0·8}O_3$ followed by a gradual decrease to $LaMn_{0·8}Co_{0·2}O_3$ perovskites due to the substitution of Co with Mn atoms [41].

The SEM analysis of the synthesized perovskites is shown in Fig. 2. It can be seen that all samples have a porous structure, which is typically observed due to the evolution of gases during the combustion synthesis process [15, 42–45]. Gas phase products such as N_2, CO_2, and also water vapor are generated during combustion and tend to escape while creating a porous network in the solid phase. Thermal effects also govern their movement during escape since the temperature cannot be expected to remain uniform throughout the entire synthesis process. These effects lead to channeling and the formation of pores, which can, to some extent, be regulated by changing the amount of gas products evolved and the heat of the combustion reaction [46]. EDX elemental analysis of each perovskite is shown in Table 1, where the ratio of Mn:Co in the perovskites is consistent with the predicted composition, confirming successful doping of the targeted amounts of Mn in the Co sites.

Among the synthesized perovskites, the $LaMn_{0.4}Co_{0.6}O_3$ showed the highest electrocatalytic activity (Figs. 5, 6, and 7; described later) for ORR, OER, and MOR in alkaline medium. Detailed characterization was performed on this

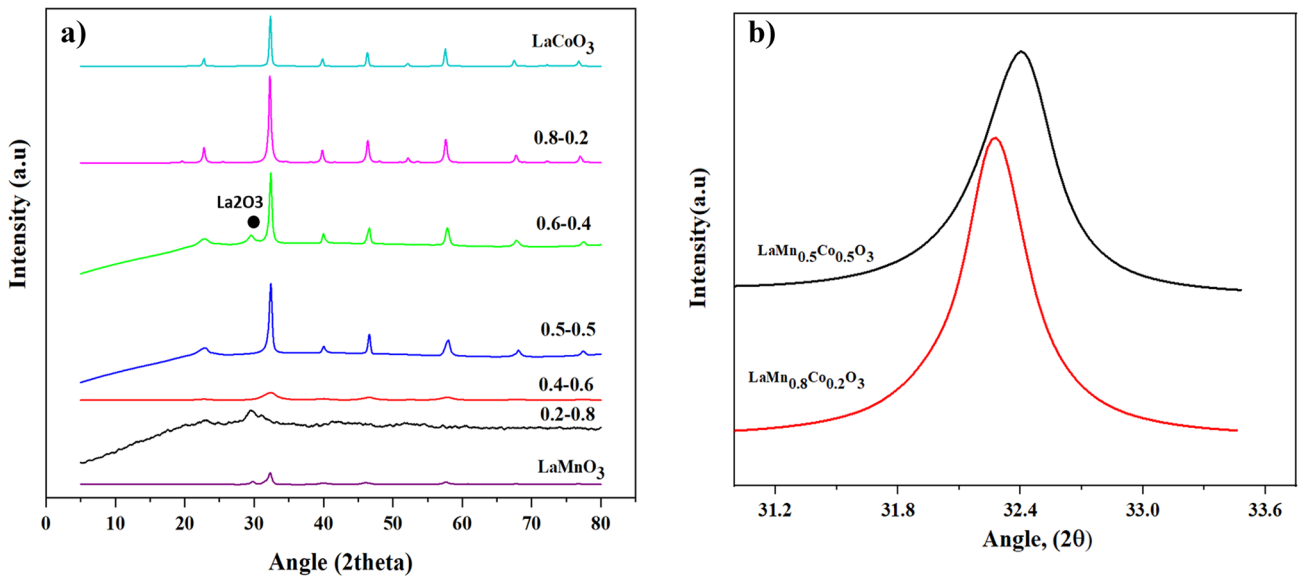

Fig. 1 **a** XRD analysis of the synthesized perovskites with different Mn to Co ratio and pure $LaMnO_3$ and $LaCoO_3$; **b** zoomed XRD profile of $LaMn_{0·8}Co_{0·2}O_3$ and $LaMn_{0·5}Co_{0·5}O_3$

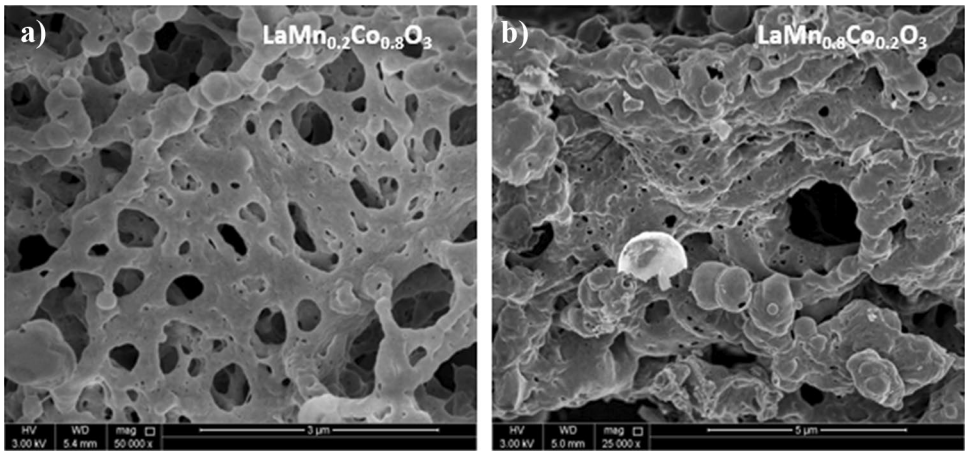

Fig. 2 SEM analysis of the synthesized perovskites. **a** $LaMn_{0.2}Co_{0.8}O_3$; **b** $LaMn_{0.8}Co_{0.2}O_3$

sample to understand the phase distribution and surface electronic properties. TEM image of $LaMn_{0.4}Co_{0.6}O_3$ perovskite in Fig. 3 shows the presence of particles in the range of 5–15 nm that are connected together in an interwoven manner. This makes the cross-linked nanoparticles network act as a three-dimensional porous structure that offers more exposed active sites for a faster electron transfer reaction and thereby enhances the overall charge transportation that is much desired in electrocatalysis. High-resolution TEM (HRTEM) in Fig. 3b shows a lattice spacing of 0.38 and 0.27 nm, which correspond to the (110) and (012) crystal planes of orthorhombic perovskite structure, and they confirm the crystallinity of the perovskite particles that was not clear in the XRD pattern of $LaMn_{0.4}Co_{0.6}O_3$.

The SAED pattern (Fig. 3c) corresponding to the selected area in Fig. 3b (circled) show spotty patterns matching with the crystalline perovskite structure, with the measured interplanar spacing associated with the crystal planes of perovskite structure. The structural alloying of the perovskite was investigated in details by performing high-angle annular dark-field scanning TEM (HAADF-STEM) imaging and EDS elemental mapping. The EDS elemental mapping of Mn, Co, and its superposition of Mn–Co and La–Mn–Co confirm that Mn and Co were atomically distributed in the nanoparticle without any clear phase separation. Similarly, the La content is uniformly dispersed all over the area and well overlapped with the transition element.

X-ray photoelectron spectroscopy (XPS) was used to identify the surface elemental composition and oxidation state of La, Mn, and Co on the perovskite samples synthesized using solution combustion synthesis. Figure 4a shows the XPS spectrum of La 3d, having two broad peaks with an energy splitting of 16.4 eV, one at lower binding energy spanned from 829 to 838 eV and another one at higher binding energy in the range of 848–856 eV, corresponding to La $3d_{5/2}$ and La $3d_{3/2}$ spectrum, respectively. Each doublet in the XPS spectrum is further split, and the intensity of splitting was found to be highest for the ratio of Mn to Co as 0.4:0.6. The splitting of doublet is common for various compounds of La such as oxides, borates, and hydroxides due to the existence of hole in La 3d electronic configuration and also it can be impacted by oxygen ligand. La 3d core level with the presence of holes lowers the 4f orbital energy level down to the Fermi level [47]. When La 3d orbital having an electronic configuration of $3d^94f^0L$ interacts with the oxygen ligand, the oxygen ligand donates an electron from its valance p orbital that is accepted by the empty *f* orbital of the lanthanum ($3d^94f^0$) to obtain a final configuration to $3d^94f^1L^-$, where the L^- indicates the valence state of oxygen ions with holes [48]. Thus, the doublet of La 3d to La $3d_{5/2}$ and La $3d_{3/2}$ exists with two configurations of $3d^94f^0L$ at lower binding energy and another satellite peak at the higher binding energy corresponding to $3d^94f^1L$. In order to obtain further insights into the doublet splitting, Fig. 4b shows the deconvolution profile of La 3d in $LaMn_{0.4}Co_{0\cdot6}O_3$, and the peaks at 832.1 (and 849.5 eV) and 837.5 eV (and 854.7 eV) associated with La $3d_{5/2}$ (and La $3d_{3/2}$) correspond to $3d^94f^0L$ and $3d^94f^1L$ configuration of La, respectively

Table 1 EDX elemental analysis of the $LaMn_xCo_{1-x}O_3$ perovskites

Catalyst	La (at.%)	Mn (at.%)	Co (at.%)	O (at.%)	C (at.%)	Mn:Co
$LaMn_{0.2}Co_{0.8}O_3$	14	3.31	13.35	48.99	19.5	0.2:0.8
$LaMn_{0.4}Co_{0.6}O_3$	13.23	5.66	9.43	52.71	18.97	0.4:0.6
$LaMn_{0.5}Co_{0.5}O_3$	13.98	8.96	8.46	50.88	17.71	0.5:0.5
$LaMn_{0.6}Co_{0.4}O_3$	13.56	8.51	5.93	52.25	19.75	0.6:0.4
$LaMn_{0.8}Co_{0.2}O_3$	15.65	13.44	3.5	51.19	16.22	0.8:0.2

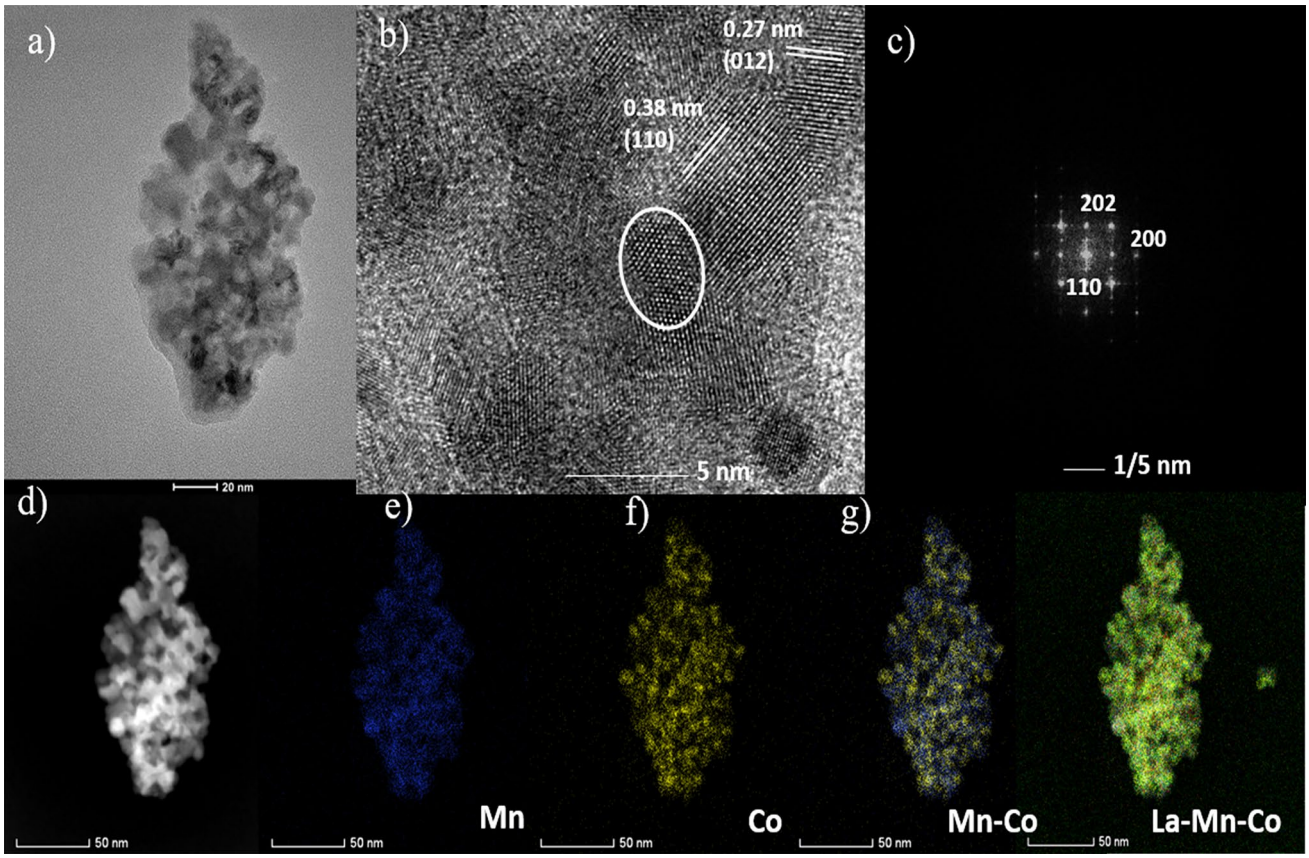

Fig. 3 **a** TEM; **b** HRETM image; **c** selected area electron diffraction (SAED) pattern of the selected region in Fig. 3b; **d–f** HAADF-EDX elemental mapping of Mn, Co, and Mn–Co and La–Mn–Co of $LaMn_{0.4}Co_{0.6}O_3$ perovskite

[49]. This indicates that $LaMn_{0.4}Co_{0\cdot6}O_3$ exhibits a stronger interaction with nearby oxygen ligands that further helps in any catalytic reaction. Figure 4c shows the Mn 2p XPS spectrum of all the Co-doped perovskite samples with binding energy in the range of 640–660 eV having doublet peaks at an energy gap of 11.8 eV, with values at 641.8 and 653.6 eV corresponding to Mn $2p_{3/2}$ and Mn $2p_{1/2}$ orbits, respectively. The deconvolution of peak fitting of Mn 2p in Fig. 4d shows the existence of a mixed valance state of Mn ions on the catalyst surface. The characteristic peak at 641.8 and 644.53 eV correspond to the presence of Mn^{3+} and Mn^{4+} ions and the composition of the Mn oxidation state varies with the substitution of Co atoms into the perovskite lattice. Likewise, the Co 2p spectrum of different La-based perovskite samples is shown in Fig. 4e with two main peaks centered at 780.2 (Mn $2p_{3/2}$) and 794.8 eV (Mn $2p_{1/2}$) with orbital energy gap of 14.6 eV between them. The deconvolution spectrum of Co 2p in Fig. 4f shows the existence of Co in two different oxidation states Co^{2+} and Co^{3+} and its ratio varies with different levels of doping [50, 51]. The Co 2p (Fig. 4c) and Mn 2p (Fig. 4e) profiles show a clear shift in the binding energy for $LaMn_{0.4}Co_{0\cdot6}O_3$, suggesting a variation in the surrounding environment of the transition metal atoms on account of an electronic coupling effect. This shows the existence of stronger electronic interaction between the transition elements on the perovskite structure that facilitates a faster electron transfer and enhances the catalytic property of the material. Also, the Fermi level of the transition metal ions gets shifted by the chemisorbed surface anions. Ghiasi and co-workers studied the effect of doping on the oxidation state of Mn and Co. The percentage of Mn^{4+} increases with an increase in Co doping, whereas the Mn^{3+} is highest when a high concentration of Mn was present in the sample. Similarly, Co^{3+} increases with Co content in the perovskite and Co^{2+} is least for the least Mn-doped catalyst [52]. The higher Co^{3+} to Co^{2+} ratio improves the oxygen absorption capability on the catalytic surface, thus improving the Co–O bond strength and promoting the ORR/OER performance. Malkhandi et al. conducted a systematic investigation on the perovskite oxides to tune the electrocatalytic activity and concluded that the relative strength of Mn–O, and Co–O bonding determines the catalytic activity [53]. Figure S3 shows the XPS O 1 s spectrum of all perovskite samples to evaluate the oxygen vacancy. It is clear to see multiple peaks in the spectrum. The peak at lower binding energy (529.5 ± 0.5 eV) corresponds to the lattice oxygen and the peak near ± 531.4 eV corresponds to non-lattice oxygen content, i.e., the oxygen-deficient region.

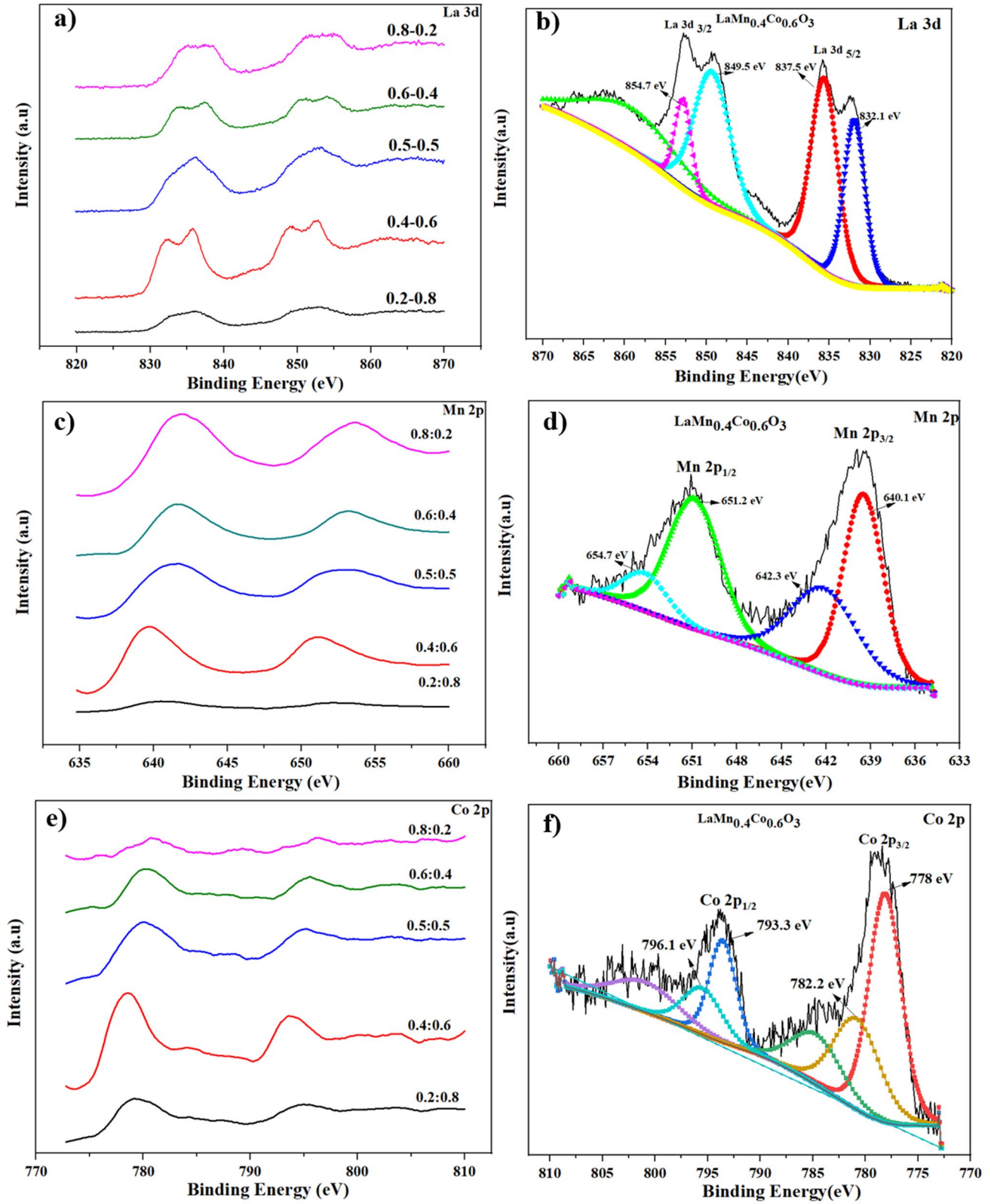

Fig. 4 XPS spectrum of **a** La 3d, **c** Mn 2p, and **e** Co 2p of all the as-synthesized perovskite catalyst. The XPS deconvolution profile of **b** La 3d, **d** Mn 2p, and **f** Co 2p correspond to $LaMn_{0.4}Co_{0\cdot6}O_3$ perovskite

The relative oxygen vacancy concentration was measured by the ratio of the area of non-lattice oxygen peak to lattice oxygen peak in the sample. In this context, the amount of oxygen vacancy is highest for $LaMn_{0.4}Co_{0\cdot6}O_3$. The non-lattice oxygen sites can absorb more oxygen species and promotes the oxidation–reduction reaction that consequently improves the electrocatalytic performance.

The electrocatalytic performance of the as-synthesized catalysts was studied by conducting cyclic voltammetry (CV) and linear sweep voltammetry (LSV) experiments in O_2-saturated 1 M KOH. The cyclic voltammetry (CV) profile of $LaMn_{0.4}Co_{0.6}O_3$ in N_2 and O_2 saturated 1 M KOH solution is shown in Fig. 5a. The current response in N_2 shows multiple strong redox peaks that are indicative of the capacitive nature of the faradaic redox reaction. The strong reduction peak around 0.72 V in the CV profile in O_2 saturated solution confirms the ORR over $LaMn_{0.4}Co_{0.6}O_3$. The ORR peak potential at 0.72 V originates due to the reaction that allows the catalysts to follow either a four-electron pathway to two-electron pathway where the oxygen molecule gets reduced with 4 electrons and 2 water molecules to generate 4 OH ions. Figure 5b shows the CV of all the La–Mn–Co-based perovskite catalyst with a clear shift of the reduction peak toward a positive potential for $LaMn_{0.4}Co_{0.6}O_3$, confirming a better interaction of absorbed oxygenated species for Mn to Co ratio of 0.4:0.6 toward ORR. The CV profile in a wider range between 0.12 and 1.92 V in Fig. 5c proves the activity of the catalysts for oxygen evolution reaction (OER) as well. The greater current response of $LaMn_{0.4}Co_{0.6}O_3$ catalysts describes its bifunctional nature for ORR and OER performance. The bifunctionality was further confirmed using linear sweep voltammetry (LSV) analysis performed

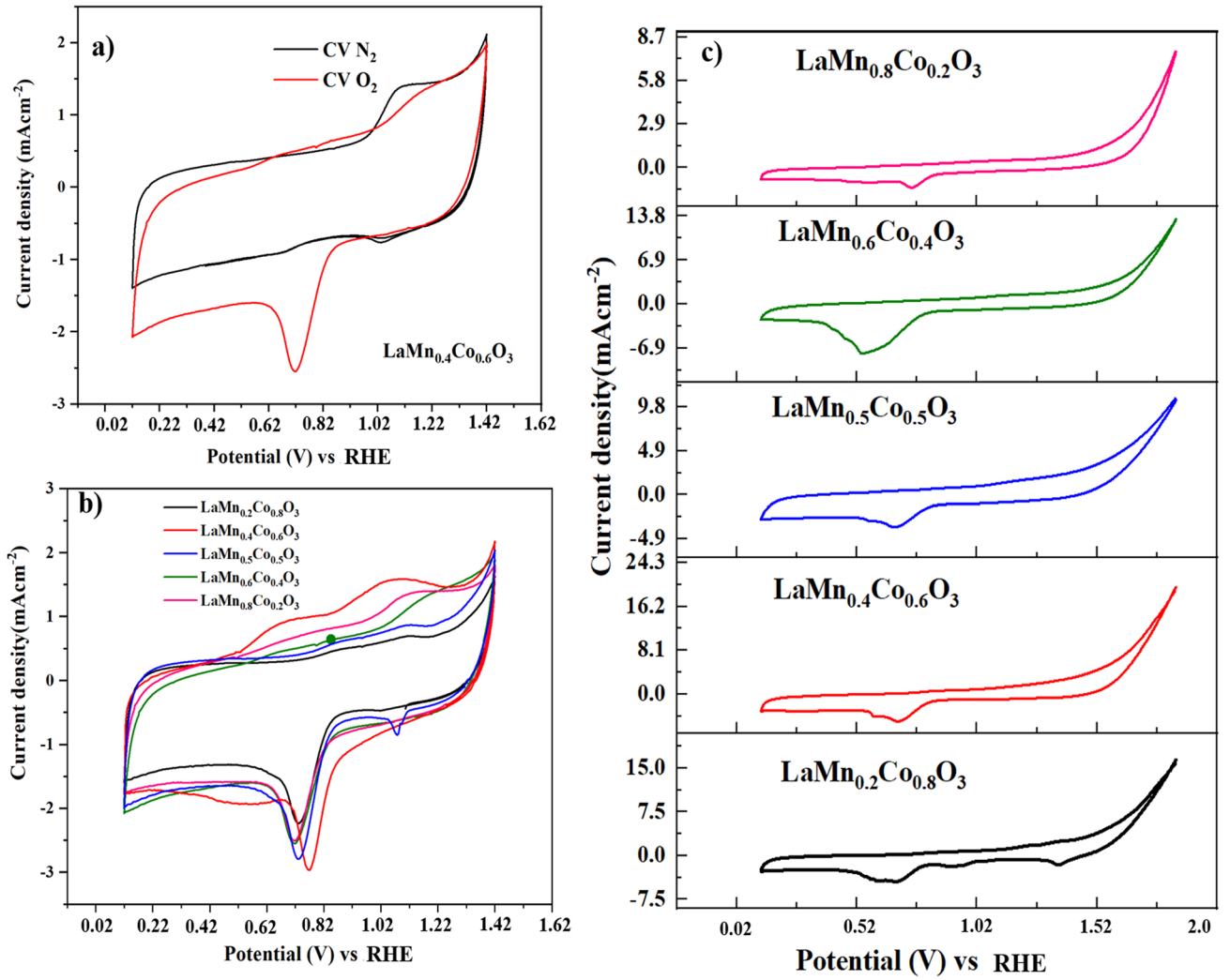

Fig. 5 **a** Cyclic voltammogram of $LaMn_{0.4}Co_{0.6}O_3$ in N_2 and O_2 saturated 1 M KOH solution at 50 mVs^{-1} scan rates; **b** Cyclic voltammogram of La perovskites doped with Mn and Co at different ratios in O_2 saturated 1 M KOH solution; **c** CV profile of all the perovskite catalyst to confirm the activity toward oxygen evolution reaction in 1 M KOH solution

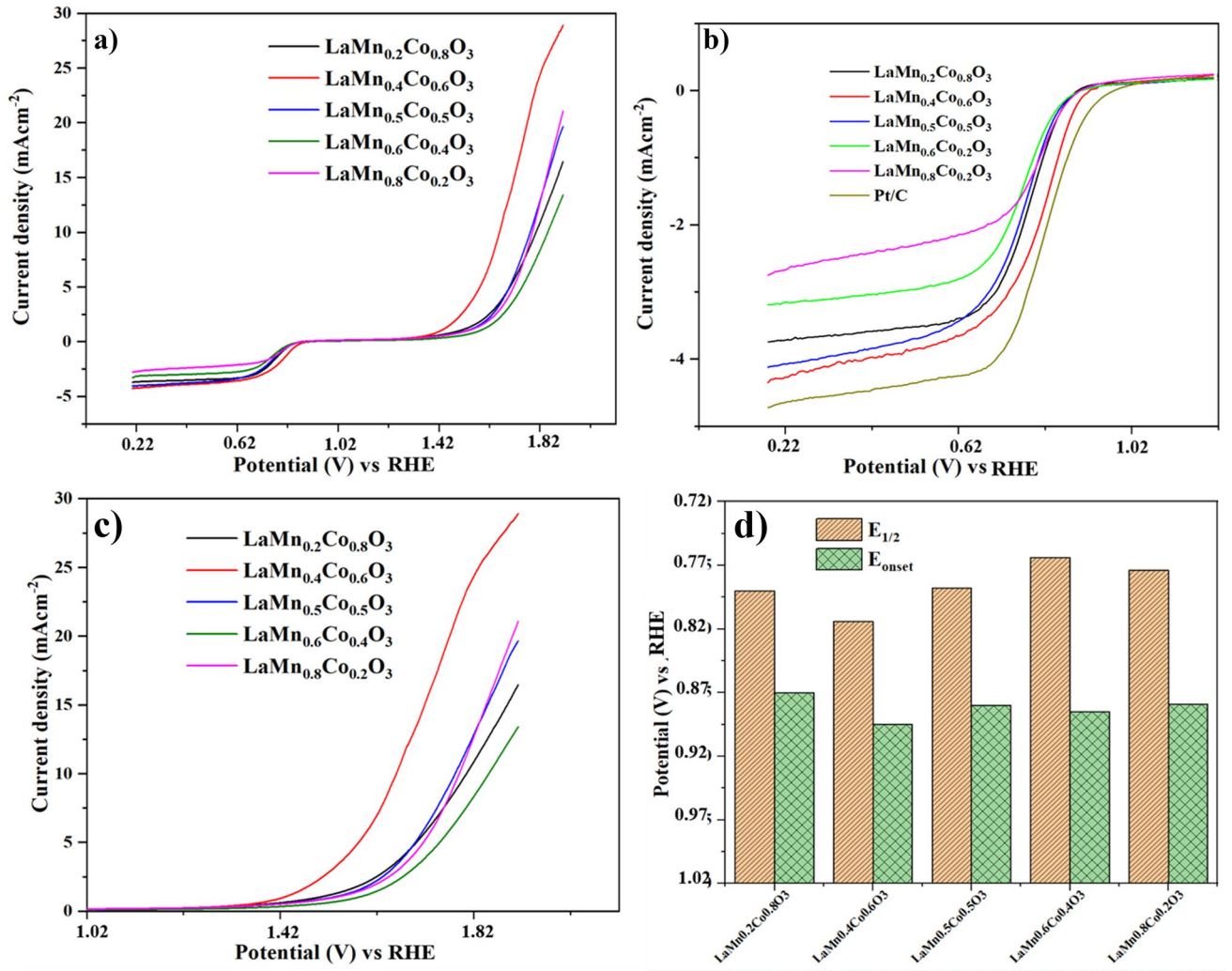

Fig. 6 **a** Linear sweep voltammogram (LSV) of La–Mn–Co-based perovskites tested in O_2 saturated 1 M KOH solution at a scan rate of 5 mVs^{-1} in the potential range of − 0.8 to 0.8 V at 1600 rpm of working electrode. Zoomed LSV profile for **b** oxygen reduction reaction of perovskite and commercial Pt/C, **c** oxygen evolution reaction, and the bar plot in **d** shows the comparison of half wave potential ($E_{1/2}$) and onset potential (E_{onset}) of the perovskite catalyst

in O_2 saturated 1 M KOH at 5 mVs^{-1} scan rates at 1600 rpm as shown in Fig. 6a. The ORR analysis of the catalysts shows improved performance on $LaMn_{0.4}Co_{0.6}O_3$ in terms of current density, half wave potential, and onset potential. The limiting current density was highest for $LaMn_{0.4}Co_{0.6}O_3$ compared to the other Mn–Co ratio. Moreover, the onset potential of $LaMn_{0.4}Co_{0.6}O_3$ (0.91 V) also shifted toward a positive potential than other Mn:Co ratios and the value is more comparable to the commercial Pt/C (0.95 V) as we reported before [51]. The two main parameters that govern the quality of oxygen transfer on the surface of the catalyst are mass activity and kinetic current density. The mass activity measured for $LaMn_{0.4}Co_{0.6}O_3$ at 0.9 V was found to be highest at 23.2 mAmg^{-1} that is very close to the commercial Pt/C reported elsewhere [54]. The kinetic current density was calculated based on Eq. (3) at 0.8 V and the obtained values are in increasing order of 7.2 mAcm^{-2}, 8.6 mAcm^{-2}, 10.6 mAcm^{-2}, 11.8 mAcm^{-2}, and 15.2 mAcm^{-2}, which correspond to $LaMn_{0.6}Co_{0.4}O_3$, $LaMn_{0.8}Co_{0.2}O_3$, $LaMn_{0.2}Co_{0.8}O_3$, $LaMn_{0.5}Co_{0.5}O_3$, and $LaMn_{0.4}Co_{0.6}O_3$, respectively, affirming the highest kinetic performance of Mn:Co ratio of 0.4:0.6.

OER in the potential range of 1.22 to 1.82 V in Fig. 6c exhibits the highest current density and faster anodic current response for $LaMn_{0.4}Co_{0.6}O_3$ when compared to other catalysts. The faster anodic response of the catalyst was described by the shorter potential difference (ΔE) between E_{onset} in the cathodic reaction and the potential at which the current start increases in the anodic reaction. A promising reversible oxygen electrocatalyst will exhibit a shorter ΔE value to indicate its bifunctional characteristics. The OER current density at 1.62 V was 2.6 mAcm^{-2}, 7.3 mAcm^{-2}, 2.4 mAcm^{-2}, 1.6 mAcm^{-2},

and 2.1 $mAcm^{-2}$ for $LaMn_{0.2}Co_{0.8}O_3$, $LaMn_{0.4}Co_{0.6}O_3$, $LaMn_{0.5}Co_{0.5}O_3$, $LaMn_{0.6}Co_{0.4}O_3$, and $LaMn_{0.8}Co_{0.2}O_3$ reconfirm the highest activity of La perovskites with Mn:Co ratio of 0.4:0.6. Shen et al. reported the reversible surface reconstruction of perovskite structure after OER into the oxyhydroxide formation [55]. They proposed a mechanism of reversible oxyhydroxide formation on the spinel Co_3O_4 surface and can be relative to the presence of redox couple Co^{3+}/Co^{2+} present in tetrahedral coordination in Co_3O_4. If the applied potential is greater than the redox potential of Co^{3+}/Co^{2+}, the Co^{2+} on the surface gets oxidized to form Co^{3+} accompanied by the transformation of oxyhydroxide species. The post-analysis of the catalyst is recommended in these circumstances, and it is considered to be the future scope of the study.

The bar plot in Fig. 6d compares the half-wave potential and the onset potential for all the tested catalysts, and it is clear that both values shifted toward a positive potential owing to the improved performance, and the positivity of the half-wave potential is in the order of $LaMn_{0.6}Co_{0.4}O_3 < LaMn_{0.8}Co_{0.2}O_3 < LaMn_{0.2}Co_{0.8}O_3 < LaMn_{0.5}Co_{0.5}O_3 < LaMn_{0.4}Co_{0.6}O_3$.

The polarization curve for $LaMn_{0.4}Co_{0.6}O_3$ at different rotation speeds (400 to 1600 rpm) shown in Fig. S4(a) shows an increase in the current density profile with an increase in rotator speed owing to the rapid transfer of the dissolved oxygen in the electrolyte to the catalyst interface thereby speeding up the reaction mechanism. The Koutecky–Levich (KL) plot in Fig. S4(b) follows excellent linearity for all the tested catalysts indicating the first-order kinetics for the oxygen reduction reaction. The overall electron transfer calculated from Eq. (4) confirms a direct four-electron transfer mechanism for ORR where the oxygen directly converts to water molecules over the electrode surface. The number of electrons gets exchanged per oxygen molecule on the active sites for the ORR was calculated as 3.98, 3.92, 3.86, 3.81, and 3.79 corresponding to $LaMn_{0.4}Co_{0.6}O_3$, $LaMn_{0.5}Co_{0.5}O_3$, $LaMn_{0.2}Co_{0.8}O_3$, $LaMn_{0.8}Co_{0.2}O_3$, and $LaMn_{0.6}Co_{0.4}O_3$, respectively, that indicates the highest electron transfer ability for $LaMn_{0.4}Co_{0.6}O_3$ perovskite.

Tafel plot can be plotted with kinetic current density calculated from Eq. (3) on the *x*-axis and the applied potential on the *y*-axis in order to understand the electro kinetics of the anodic and cathodic oxygen electrocatalysts involved. The Tafel plot on the cathodic reaction consists of two slopes, one at a lower potential corresponding to Temkin isotherm and the other at a higher potential corresponding to Langmuir isotherm, as in Fig. S5. In general, the oxygen electrocatalyst holding a higher slope value at lower potential and lower slope at higher potential is considered an ideal electrocatalyst. The slope values corresponding to each isotherm are shown in Table S1, and while considering the correlation of slope value and the performance of the catalyst, it is confirmed that $LaMn_{0.4}Co_{0.6}O_3$ has improved electro kinetics and catalytic performance compared to others. The electrocatalysts were further evaluated for the methanol oxidation reaction to assess the application of the selected catalysts for methanol fuel cell.

The combustion synthesized $LaMn_xCo_{1-x}O_3$ perovskites were further studied using cyclic voltammetry for MOR within a potential range of 1.62 to 0.42 V versus Ag/AgCl reference electrode. The initial and final potentials were set at 1.02 and 1.52 V, and the scan rate employed for the electrochemical measurements was 500 mV/s in the GCE electrodes. The plots of before and after methanol addition for all *x*-values of $LaMn_xCo_{1-x}O_3$ samples are represented in Fig. S6(a–e). No MOR activity was observed before the addition of methanol when the solution was saturated with only N_2 (black curves) and the maximum current densities at $x = 0.2$, 0.4, 0.5, 0.6, and 0.8 were found to be 1.15 mA cm^{-2}, 0.64 mA cm^{-2}, 0.53 mA cm^{-2}, 0.72 mA cm^{-2}, and 0.38 mA cm^{-2}, respectively. After the addition of methanol (1 M), an increase in the current density peak was observed for all the compositions as seen from the red curves in Fig. S6(a–e). The highest current density value after methanol addition was 4.84 mA cm^{-2}, which was achieved at $x = 0.4$ as seen in Fig. 7 (a). Similarly, for other ratios at $x = 0.2$, 0.5, 0.6, and 0.8, the maximum current density value increased to 2.42 mA cm^{-2}, 1.47 mA cm^{-2}, 3.73 mA cm^{-2}, and 1.96 mA cm^{-2} in the methanol CV curve, respectively. Thus, the increase in the current value indicates that oxidation of methanol has occurred in the system with the aid of the electrocatalysts.

A comparative study of all samples of $LaMn_xCo_{1-x}O_3$ perovskites after methanol addition is shown in Fig. 7 (b), and the relatively higher current density value being displayed by the perovskite material with an '*x*' value of 0.4 shows that it is capable of oxidizing methanol at a faster rate than those with other values of '*x*' and is the most active among all the compositions.

Moreover, the LSV measurements for all samples of $LaMn_xCo_{1-x}O_3$ were carried out in order to analyze the MOR activity. LSV of all the samples in the potential range of 1.02 to 2 V are represented in Fig. 7(c). From the plots, it is clear that after the addition of 1 M methanol, there is a significant increase in the current densities after reaching an onset potential value. The onset potential values for $x = 0.2$, 0.4, 0.5, 0.6, and 0.8 are 1.55 V, 1.52 V, 1.65 V, 1.54 V, and 1.67 V, respectively. The early onset potential being demonstrated by the perovskite with an '*x*' value of 0.4 indicates that a relatively lower electrode potential is required for a methanol oxidation reaction to occur. In addition, this material is also capable of reaching a higher final current density value, 33.45 mA cm^{-2}, than those with other values of *x* (*x* of 0.2, 0.5, 0.6, and 0.8 displayed a final current density of 27.87, 18.74, 29.44, and 12.73 mA cm^{-2}, respectively). Thus, $LaMn_xCo_{1-x}O_3$ perovskite with $x = 0.4$ performs better

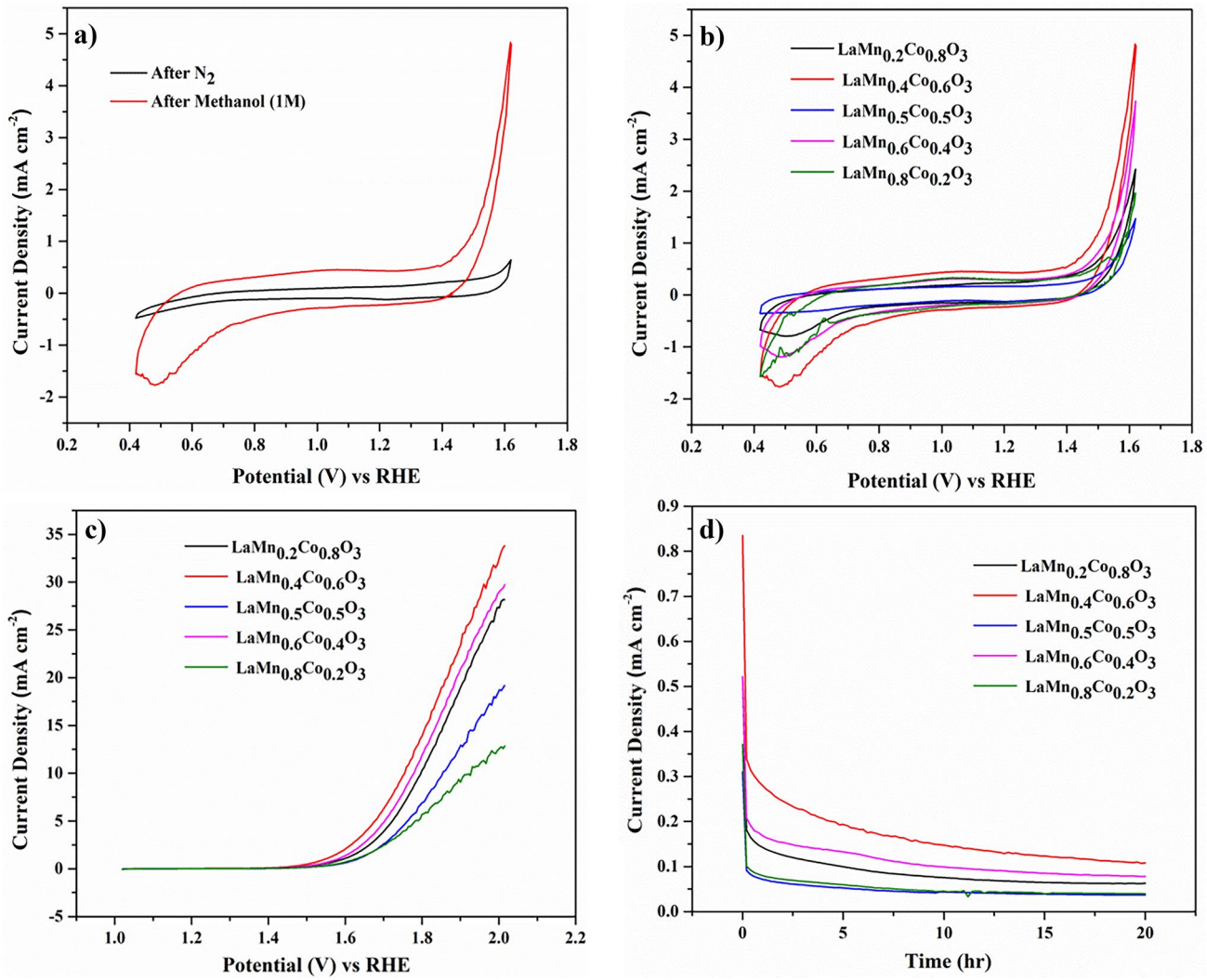

Fig. 7 **a** Cyclic voltammogram diagram after N_2 purge and methanol (1 M) of $LaMn_{0.4}Co_{0.6}O_3$, **b** CV comparison of all $LaMn_xCo_{1-x}O_3$ samples after adding methanol (1 M), **c** linear sweep voltammetry of all $LaMn_xCo_{1-x}O_3$ ($0 \le x \le 1$) after N_2 purge and methanol (1 M) in 1 M KOH electrolyte, and **d** chronoamperometry test of all $LaMn_xCo_{1-x}O_3$ in 1 M methanol and 1 M KOH electrolyte for up to 20 h

as it showed the highest current density compared to other catalysts, consistent with the results from CV. In addition, the long-term stability of different $LaMn_xCo_{1-x}O_3$ perovskites was examined using the chronoamperometry (CA) method, and the results are represented in Fig. 7 (d). The CA data of current density versus time was measured at a fixed potential of 1.52 V in 1 M methanol and 1 M KOH electrolyte at room temperature. A similar pattern is seen in all the catalysts, exhibiting MOR activity for more than 20 h after the initial sharp decrease in current density. This decrease was observed for all the samples until 150 s, which could be due to the adsorption of intermediates formed during the oxidation process. Thereafter, all the catalysts show a reasonably stable performance, where $LaMn_{0.4}Co_{0.6}O_3$ consistently maintains a higher current density compared to other samples. These results, ORR, OER, and MOR indicate the versatile nature of $LaMn_xCo_{1-x}O_3$ perovskites for driving cathodic and anodic reactions in an alkaline medium.

Conclusions

In conclusion, lanthanum-based synthetic perovskites ($LaMn_xCo_{1-x}O_3$ ($0 \le x \le 1$)) were synthesized with different ratios of Mn and Co to study their activity for ORR, OER, and MOR in an alkaline medium. The synthesized perovskites were analyzed structurally and morphologically using characterization techniques such as XRD, FTIR,

SEM, TEM, and XPS. The SEM analysis concluded that all the samples have a porous structure, while the TEM with nanoscale phase analysis showed a uniform presence of La, Mn, and Co all over the sample. XRD and TEM analysis confirmed the synthesis of perovskite structure without any phase segregation, indicating a smaller crystallite size in $LaMn_{0.4}Co_{0.6}O_3$ compared to other samples. XPS peak fitting of La_{3d}, Co_{2p}, and Mn_{2p} peaks confirms the existence of a mixed valence state. The deconvolution of Mn2p provided a signature of having Mn^{3+} and Mn^{4+} peaks, and the composition of each oxidation states varied with the amount of Co doping. The Mn^{4+} and Co^{3+} contents are highest at higher Co doping, and studies showed the significance of having higher oxidation state toward catalytic properties. A shift in the binding energy of Co 2p and Mn 2p was observed for $LaMn_{0.4}Co_{0\cdot6}O_3$, indicating a strong interaction with the nearby atoms that resulted in enhanced electrocatalytic activity. Detailed electrochemical studies in an alkaline medium were conducted to investigate the activity and stability of the catalysts using CV, LSV, and CA techniques for ORR, OER, and MOR. The $LaMn_xCo_{1-x}O_3$ perovskite with $x=0.4$ showed the highest current density and stability compared to the other catalysts for all three reactions.

Supplementary Information The online version contains supplementary material available at https://doi.org/10.1007/s12678-022-00772-0.

Acknowledgements This work was made possible by the NPRP grant (NPRP13S-0109-200029) and UREP grant (UREP24-001-2-001) from the Qatar National Research Fund (a member of Qatar Foundation). The statements made herein are solely the responsibility of the authors. The authors also acknowledge the Center for Advanced Materials (CAM), Gas Processing Center (GPC), and the Central Laboratory Unit (CLU) at Qatar University for providing services related to XRD, XPS, and electron microscopy analysis. The authors would also like to thank QEERI Core Labs for the TEM characterization.

Funding Open Access funding provided by the Qatar National Library.

Declarations

Conflict of Interest The authors declare no competing interests.

References

1. Z. Wang, X. Zhang, A. Rezazadeh, Energy Rep. **7**, 2594 (2021)
2. L. Carrette, K.A. Friedrich, U. Stimming, Fuel cells **1**, 5 (2001)
3. L.K. Verma, J. Power Sources **86**, 464 (2000)
4. M. Baldauf, W. Preidel, J. Power Sources **84**, 161 (1999)
5. D. Ham, J. Lee, Energies (Basel) **2**, 873 (2009)
6. S.K. Kamarudin, F. Achmad, W.R.W. Daud, Int. J. Hydrogen Energy **34**, 6902 (2009)
7. A. Ashok, A. Kumar, Int. J. Hydrogen Energy **46**, 4788 (2021)
8. Z. Wei, J. Sun, Y. Li, A.K. Datye, Y. Wang, Chem. Soc. Rev. **41**, 7994 (2012)
9. M. Sankar, N. Dimitratos, P.J. Miedziak, P.P. Wells, C.J. Kiely, G.J. Hutchings, Chem. Soc. Rev. **41**, 8099 (2012)
10. E.E. Wolf, A. Kumar, A.S. Mukasyan, In 297–346 (2019)
11. A. Yuda, A. Ashok, A. Kumar, Catalysis Rev. - Sci. Eng. (2020)
12. A. Ashok, A. Kumar, A. Yuda, A. Al Ashraf, Int. J. Hydr. Energ. (2021)
13. E.A. Batista, G.R.P. Malpass, A.J. Motheo, T. Iwasita, J. Electroanal. Chem. (2004)
14. S. Wasmus, A. Küver, J. Electroanal. Chem. (1999)
15. A. Ashok, A. Kumar, R.R. Bhosale, F. Almomani, S.S. Malik, S. Suslov, F. Tarlochan, J. Electroanal. Chem. **809**, 22 (2018)
16. S. Chen, M. Li, M. Gao, J. Jin, M.A. van Spronsen, M.B. Salmeron, P. Yang, Nano Lett. **20**, 1974 (2020)
17. E. Antolini, J.R.C. Salgado, E.R. Gonzalez, Appl. Catal. B **63**, 137 (2006)
18. K. Scott, L. Xing, In 145–196 (2012)
19. L. Niu, Q. Li, F. Wei, S. Wu, P. Liu, X. Cao, J. Electroanal. Chem. (2005)
20. S. Royer, D. Duprez, F. Can, X. Courtois, C. Batiot-Dupeyrat, S. Laassiri, H. Alamdari, ChemInform **45**, (2014)
21. M. Zhang, G. Jeerh, P. Zou, R. Lan, M. Wang, H. Wang, S. Tao, Materials today (2021)
22. G. George, S. R. Ede, Z. Luo, In Fundamentals of perovskite oxides (CRC Press, 2020), pp 273–335 (2020)
23. S.B. Adler, Solid State Ionics **111**, 125 (1998)
24. A. Galal, N. F. Atta, M. A. Hefnawy, J. Electroanal. Chem. (2020)
25. T.Q.N. Tran, S.W. Yoon, B.J. Park, H.H. Yoon, J. Electroanal. Chem. (2018)
26. N. Erdenee, U. Enkhnaran, S. Galsan, A. Pagvajav, J. Nanomater. **2017**, 1 (2017)
27. Y. Sim, D. Kwon, S. An, J.-M. Ha, T.-S. Oh, J.C. Jung, Molecular catalysis **489**, 110925 (2020)
28. M.A. Peña, J.L.G. Fierro, Chem. Rev. **101**, 1981 (2001)
29. K. Deshpande, A. Mukasyan, A. Varma, J. Power Sources **158**, 60 (2006)
30. J.O. Bockris, T. Otagawa, V. Young, J. Electroanal. Chem. Interfacial Electrochem. **150**, 633 (1983)
31. Z. Chen, J. Hu, Z. Lu, X. He, Ceram. Int. **37**, 2359 (2011)
32. Y. Wen, C. Zhang, H. He, Y. Yu, Y. Teraoka, Catal. Today **126**, 400 (2007)
33. A. Ashok, A. Kumar, R.R. Bhosale, M.A.H. Saleh, U.K. Ghosh, M. Al-Marri, F.A. Almomani, M.M. Khader, F. Tarlochan, Ceram. Int. **42**, 12771 (2016)
34. A. Ashok, A. Kumar, R.R. Bhosale, M.A.H. Saleh, L.J.P. van den Broeke, RSC Adv. **5**, 28703 (2015)
35. A. Kumar, A. Ashok, R.R. Bhosale, M.A.H. Saleh, F.A. Almomani, M. Al-Marri, M.M. Khader, F. Tarlochan, Catal. Lett. **146**, 778 (2016)
36. A. Cross, A. Kumar, E.E. Wolf, A.S. Mukasyan, Ind. Eng. Chem. Res. **51**, 12004 (2012)

37. A. Kumar, A.S. Mukasyan, E.E. Wolf, Appl. Catal. A **372**, 175 (2010)
38. A. Kumar, A.S. Mukasyan, E.E. Wolf, Appl. Catal. A **401**, 20 (2011)
39. C. Autret, J. Hejtmánek, K. Knížek, M. Maryško, Z. Jirák, M. Dlouhá, S. Vratislav, J. phys. condensed matt. (2005)
40. S.A. Hosseini, D. Salari, A. Niaei, S.A. Oskoui, J. Industrial and Eng. Chem. (2013)
41. S.A. Hosseini, M.T. Sadeghi, A. Alemi, A. Niaei, D. Salari, L. Kafi-Ahmadi, Cuihua Xuebao/Chinese J. Catalysis (2010)
42. I.S. Altman, I.E. Agranovski, M. Choi, Appl. Phys. Lett. **87**, 053104 (2005)
43. A. Ashok, A. Kumar, J. Ponraj, S.A. Mansour, J. Electrochem. Soc. **167**, 054507 (2020)
44. A. Ashok, A. Kumar, J. Ponraj, S.A. Mansour, F. Tarlochan, Int. J. Hydrogen Energy **44**, 16603 (2019)
45. A. Ashok, A. Kumar, J. Ponraj, S.A. Mansour, F. Tarlochan, Catalysis today (2020)
46. A. Ashok, A. Kumar, M.A. Matin, F. Tarlochan, J. Electroanal. Chem. **844**, 66 (2019)
47. C.L. Perkins, M. Trenary, T. Tanaka, S. Otani, Surface Sci. (1999)
48. E. Talik, A. Novosselov, M. Kulpa, A. Pajaczkowska, J. Alloys and Compounds (2001)
49. N. Sethulakshmi, A.N. Unnimaya, I.A. Al-Omari, S. Al-Harthi, S. Sagar, S. Thomas, G. Srinivasan, M.R. Anantharaman, J. Magnetism and Magnetic Mater. (2015)
50. A. Ashok, A. Kumar, J. Ponraj, S.A. Mansour, Carbon NY (2020)
51. A. Ashok, A. Kumar, M.A. Matin, F. Tarlochan, ACS Omega **3**, 7745 (2018)
52. M. Ghiasi, M.U. Delgado-Jaime, A. Malekzadeh, R.P. Wang, P.S. Miedema, M. Beye, F.M.F. De Groot, J. Phys. Chem. C (2016)
53. S. Malkhandi, P. Trinh, A.K. Manohar, A. Manivannan, M. Balasubramanian, G.K.S. Prakash, S.R. Narayanan, J. Phys. Chem. C (2015)
54. A.M. Jasim, G. Xu, S. Al-Salihi, Y. Xing, ChemistrySelect (2020)
55. T.H. Shen, L. Spillane, J. Vavra, T.H.M., Peng, J., Y. Shao-Horn, & V. Tileli, Journal of the American Chemical Society (2020).